LAWRENCE
LIVERMORE
NATIONAL
LABORATORY

UCRL-TR-203156

High-pressure, high-strain-rate materials effects

D.H. Kalantar, J. Belak, E. Bringa, K. Budil, J. Colvin, M. Kumar, M.A. Meyers, K. Rosolankova, R. Rudd, M. Schneider, J. Stölken, J.S. Wark

March 4, 2004

Abstract

A 3-year LDRD-ER project to study the response of shocked materials at high pressure and high strain rate has concluded. This project involved a coordinated effort to study single crystal samples that were shock loaded by direct laser irradiation, in-situ and post-recovery measurements, and molecular dynamics and continuum modeling.

Laser-based shock experiments have been conducted to study the dynamic response of materials under shock loading materials at a high strain-rate. Experiments were conducted at pressures above the published Hugoniot Elastic Limit (HEL). The residual deformation present in recovered samples was characterized by transmission electron microscopy, and the response of the shocked lattice during shock loading was measured by in-situ x-ray diffraction. Static film and x-ray streak cameras recorded x-rays diffracted from lattice planes of Cu and Si both parallel and perpendicular to the shock direction. Experiments were also conducted using a wide-angle detector to record x-rays diffracted from multiple lattice planes simultaneously. This data showed uniaxial compression of Si (100) along the shock direction and 3-dimensional compression of Cu (100). In the case of the Si diffraction, there was a multiple wave structure observed. We present results of shocked Si and Cu obtained with a new large angle diffraction diagnostic, and discuss the results in the context of detailed molecular dynamics simulations and post-processing.

Contents:

Technical report

Introduction

The dynamics of material response to pressure loading depends on the pressure and strain rate. Processes may be extremely slow, such as the movement of the tectonic plates on the earth (10^{-17}-10^{-14} s^{-1}) [1], or fast, such as the dynamic response of materials under shock loading (10^{5}-10^{7} s^{-1} or higher) [2]. There are experimental techniques that allow us to access these different regimes of pressure and strain rate. The diamond anvil cell is an example for slow isotropic compressions up to the 100 GPa (1 Mbar) range. For dynamic processes, there are Hopkinson bar, gun, and high explosive (HE) facilities. In these, the pressures are typically <100 GPa, and only moderate strain rates (10^{3}-10^{6}) are accessed. In addition, pulsed power [3] and intense lasers [4] provide a source of high energy density to compress materials at moderate pressures (>100 GPa) while remaining solid.

The response of a solid material under compression is typically described with a constitutive model, such as the Steinberg-Guinan model [5] or the Steinberg-Lund model [2]. These are semi-empirical models for the shear stress and yield stress. They are elastic-perfectly plastic models, which means that when the applied stress exceeds the yield stress, the shear stress remains constant and equal to the yield stress with increasing strain. The material responds elastically up to the point where the stress exceeds the yield stress, at which point, it yields to plastic flow. This formulation includes the enhancement of strength due to pressure, as well as parameters to represent work hardening and thermal softening. However, these models do not include any details of the microstructure that may affect the dynamic behavior of the material.

In fact, materials have a lattice and microstructure, and details of this microstructure affect the dynamics of the material response due to stress loading. Material structure occurs over a range of scale-lengths from the atomic scale to the continuum. Pre-existing dislocation networks, grain boundaries, or even the lattice direction relative to the shock loading direction affect the response. Solids undergo deformation by generating and propagating lattice dislocations. This same process occurs under shock loading at high pressure. [6] Microscopically, solid-state plastic flow is the result of rearrangement of the lattice structure by transport of these dislocations. The number density of dislocations that are generated and the speed with which they propagate vary with lattice orientation and depend on the material, the rate of the applied strain, as well as the initial microstructure and existing dislocation structures.

Shock experiments are traditionally diagnosed with techniques such as recovery and post-shock microstructural analysis, free surface breakout velocity, or in-situ particle velocity or stress gauge measurements. In the case of the residual deformation analysis, the structure that is observed is the result of shock loading, release, and subsequent thermal recovery. This means for example, that the post-shock dislocation density does not represent the actual density during shock loading, although the characteristic deformation structures does represent the type of deformation that occurs.

Free-surface velocity is measured using an interferometer (VISAR). The wave profiles that are obtained are fit with continuum simulations in order to infer continuum model parameters for material response. In-situ gauge measurements are possible only for low stresses and slow time scales.

To study the detailed response of a material to shock loading, it is important to study the response of the material during shock loading with a technique such as *in-situ* dynamic x-ray diffraction [7-10]. This technique has been applied on gas gun facilities, as well as on laser-based experiments. In this discussion, we focus on laser-based

experiments [4, 11,12] since high-energy lasers provide a capability to access high-pressure states of material and simultaneously provide x-ray diagnostic capabilities.

In this report, we present results from a 3-year LDRD project that integrated a suite of techniques to understand the dynamic response of shocked materials compressed at high strain rate by laser-irradiation. We describe a series of laser-based shock measurements, including recovery and micro-structural analysis, and wave profile measurements. We also describe the dynamic technique of in-situ x-ray diffraction to probe the lattice response directly. We present results of shocked Si and Cu obtained with a new large angle diffraction diagnostic, and discuss the results in the context of detailed molecular dynamics simulations and post-processing

Residual deformation by micro-structural analysis

One approach to investigate the deformation mechanisms that determine material response is transmission electron microscopy (TEM). Material samples that are subjected to shock loading are recovered and the microstructure is studied. Single crystal Cu and Cu-Al alloy samples have been shocked and recovered using the OMEGA and Janus lasers. In these experiments, the 0.5-5.0 mm thick disks had a [001] or [134] lattice orientation relative to the shock direction. A single high intensity laser beam was used to generate the shock pressure by direct laser ablation of the surface of the single crystal sample. A strong shock was generated at the surface of the single crystal sample with peak pressures of up to 100 GPa by using a total of up to 320 J of laser energy. The pulses were typically 2-3.5 ns in duration with 1-3 mm spot size.

In the laser experiments, the pulse duration is short. A strong shock is generated that is closely followed by a release wave as it propagates into bulk of the sample. This results in a decaying shock wave that broadens is time, such as illustrated by the

calculation shown in Fig. 1. The samples were recovered in a reservoir of low-density foam. They were sliced into thin sections and mechanically ground to a thickness of 100 μm. These samples were then prepared for transmission electron microscopy using an electropolishing solution.

The residual microstructure evident in the recovered samples of single crystal Cu [001] and [134] were compared at a range of pressures. [13-15] The results show residual structure that is similar to that observed in lower strain rate shock experiments. Examples of the results obtained at a range of shock pressures are described below.

A. Deformation Microstructure of Specimens Shocked at 20 GPa (70 J)

The [001] orientation shocked at 20 GPa contains a well-defined cellular organization of dislocations with average cell size diameter between 0.2 and 0.3 μm (Fig. 2a). The microstructure was homogeneous throughout the sample. Qualitatively, these results confirm previous observations in shock experiments with a pulse duration that is longer by a factor of 10 to 100. [16] The predicted cell size from Murr's data, [17] at a pressure of 12 GPa, is 0.4 μm, and for 20 GPa, it is 0.25 μm.

The [134] orientation shocked at 20 GPa contains a similar well-defined cellular network comprised of dislocations with a slightly larger (0.3 to 0.4 μm) average cell size (Fig. 2b). The dislocation density is on the order of 10^{13} m^{-2} . The cells are comprised primarily of three separate dislocation systems and slip systems that are activated where the resolved shear stress exceeds the critical value for most of the potential systems.

B. Deformation Microstructure of Specimens Shocked at 40 GPa (200 J)

For the [001] orientation, this intermediate energy input creates dense dislocation tangles, stacking faults, and microtwins. Figure 3a shows stacking faults and dislocation tangles marked as SF and DT. There are no readily discernible dislocation cells.

Furthermore, the observed deformation substructure appears uniform around the thin foil perforation. These features are significantly different than the deformation substructure observed at the lower laser energy (Fig. 2a) in what can be construed as a pressure-dependent change in the deformation mechanism.

For the [134] orientation, the deformation substructure continues to be cellular, albeit finer at a 0.15 μm average cell size and a significantly higher dislocation density (10^{14} m^{-2}, Fig. 3b). This is in direct contrast to the mechanism change observed in [001]. Again, three slip systems dominate the deformation substructure. A large number of loops are also visible. These were found to contribute to the cell walls and were commonly observed within the cells in a very low concentration.

C. Deformation Microstructure of Specimens Shocked at 60 GPa (300 J)

The deformation microstructure of the [001] orientation shocked at 60 GPa consists of a high density of microtwins and laths (Fig. 4). The deformation is not uniform around the perforation, with the microtwins situated closer to the center of the sample and the laths away from the center. Two sets of microtwins are observed in the thin foils (not shown here) aligned along orthogonal [220] directions in roughly the same proportion.

Unlike the microtwins, the laths are elongated close to <220>. In some regions, they are aligned along [-220] and, in others, along [220]. The intermediate area shows laths misoriented from [220]. The interface between laths is parallel to [001] and therefore uniquely different from microtwins. In fact, on rare occasions, we observe laths containing some micro-twins (Fig. 4b). These features are consistent with the "wavy sub-grains" observed after high-pressure shock compression by Murr [16] (in particular, note similarities with Figs 34 and 35 of Reference 16). This structure is also analogous to the one observed by Gray [18] in specimens where the residual strain was high. Thus, it is suggested that the substructures revealed by Fig. 4 are due to thermal recovery of the

shock-induced microstructure. The orientation close to {111} of the boundaries is a residue of the original twin boundaries. This microstructure represents the recovered state of a heavily twinned and dislocated structure.

For the [134] orientation, the deformation substructure continues to be dominated by a dense cellular network of dislocations with regions of micro-twins. Under these conditions, the cell size is smaller than 100 nm. These results are consistent throughout the thin areas examined. Micro-twins are also observed within the sample with lengths ranging from 50 nm to 1 μm and (200 to 300 nm average) and widths of 20 to 30 nm.

It was found that the [001] deformation substructure evolution is systematic. As pressure increases, dislocation density increases and average cell size decreases until a critical density occurs and stacking faults form. At higher pressures, twins are widely observed. The evolution of the substructure in [134] is substantially different. At lower pressures, changes in dislocation densities and cell sizes are similar; however, twinning is found only sporadically at the highest pressure of 60 GPa. Stacking faults are also a rare occurrence in the [134] orientation.

In these laser experiments, the peak stresses were simulated with a 1-dimensional hydrodynamics code. However, the laser focal spot was 1 mm in diameter, and the single crystal samples were 3.0 mm in diameter. There are effects due to the 2-dimensional release of the stress, but the residual microstructure is similar to that observed in other shock loading experiments. [14] In fact, since the materials undergo compression, relaxation, and subsequent recovery, the residual deformation does not quantitatively represent the deformation under shock compression. There is residual deformation frozen in that is suggestive of the mechanisms that occurred during shock loading, but to fully capture the dynamic response of shocked materials, it is necessary to develop time-resolved measurements.

VISAR wave profile measurements

Free surface wave profile measurements are used in traditional and laser-based experiments to provide time-resolved information about the shock profile. This technique uses a line imaging VISAR [19] coupled to an optical streak camera. Measurements of the shock wave profile have been made on release from a number of different single crystals, including Si (001) and Cu (001), and from poly-crystalline materials at OMEGA. Information on the bulk material properties is obtained by fitting the VISAR wave profile. One example of this is shown in Fig. 5 for Al-6061. Here, the free surface velocity obtained using a 27 J laser drive energy is modeled to infer the shear modulus, bulk modulus, and yield strength. These are obtained by evaluating a best fit for the timing and peak velocity of the elastic and plastic waves as shown in the figure. [20]

VISAR wave profiles are used to benchmark the calculated pressure profiles in the recovered samples. Free surface velocity profiles from different thickness single crystal samples ranging from 0.2 to 1.0 mm thick were used to normalize the pressure at each depth in a thick sample, validating the calculated pressure profiles such as those shown earlier in Fig. 1. Wave profiles such as this provide information on the phase diagram of the material. The two-wave structure in Fig. 5 is due to an elastic precursor followed by a plastic deformation wave. For a strong shock, a two-wave structure will also occur if there is a shock-induced phase transition. In this case, the wave profile indicates the presence of a transition, but there is no information provided on the actual lattice configuration during the shock passage.

In-situ dynamic diffraction

X-ray Bragg diffraction is a technique used to study the structure of a solid. This may be used to probe materials during shock loading to characterize the dynamic lattice response. Here, x-rays scattered from the atoms in the lattice constructively interfere when the incident angle with respect to the lattice plane satisfies the Bragg condition:

$$n\lambda = 2d \times \sin(\theta)$$

The x-rays are diffracted at an angle θ equal to the incident angle (relative to the lattice planes).

When the lattice undergoes a deformation due to shock compression, the lattice compresses, so the lattice spacing decreases. The Bragg diffraction condition is then met at a different angle determined by the new lattice spacing (Fig. 6). The technique of in-situ dynamic x-ray diffraction has been used to probe shocked single crystals with x-rays as they undergo deformation by shock compression. An x-ray source is positioned very close to the crystal so that the crystal subtends a range of angles including the new Bragg angle. The shift in diffraction angle is then recorded as a spatial shift in the diffraction signal. This shift of the diffracted x-rays is sensitive to the strain in the lattice as it deforms.

Experiments were conducted on the Nova and OMEGA lasers to study the shock response of Si and Cu by recording x-rays diffracted from specific lattice planes both parallel and perpendicular to the shock direction. In these experiments, the single crystal samples were approximately 2 mm in size, with a thickness of 40 μm for the Si and 2 μm for the Cu. The single crystal was shock loaded either by indirect (x-ray) drive, or direct (laser) drive, and the sample was probed using x-rays generated by high intensity beams incident on a thin metal foil. A nearly monochromatic source of x-rays

was created. These x-rays were then diffracted from the lattice planes of the crystal and recorded on both static film and x-ray streak cameras.

X-rays diffracted from the [004] planes of Si and [002] planes of Cu parallel to the shock propagation direction in the crystal were recorded with one detector. X-rays diffracted from the orthogonal [040] planes on Si and [020] planes of Cu were recorded with a separate detector.

In the case of single crystal Si [001], the sample was shock loaded to pressures up to approximately 22 GPa. X-rays diffracted from the [004] planes showed a dynamic response as the Bragg angle shifted, as illustrated in Fig. 7. The shift of 1.85 Å x-rays from a Bragg angle of 42.95° to 46.72° indicates a compression of the 2d lattice spacing of approximately 6.4% along the shock direction. Simultaneous measurements of the orthogonal [040] lattice planes showed no response to the shock loading. In this case, the Si appears to respond uniaxially.

In the case of the single crystal Cu, the crystal foils were shock compressed to a peak pressure of approximately 20 GPa. X-rays diffracted from the [002] and [020] lattice planes showed a compression of approximately 2.5-3.0%, as illustrated in Fig. 8. In this case, the broadening of the signal is thought to be due to a high density of dislocations as well as structure in the shock due to the laser drive on the very thin samples. The observed compression in both the Bragg and Laue measurements is consistent with a fully 3-dimensional compression of the Cu, and with the shock Hugoniot for Cu at this pressure. This volumetric compression of nearly 10% is a result of the local rearrangement of the lattice under compression due to the generation and propagation of dislocations. [6]

The difference in the response of Si and Cu may be explained by the time-scale of the experiment, and the characteristic velocity for dislocations in the two materials. There is a 6-order of magnitude difference in the dislocation velocity for Si and Cu. [21]

Based on an upper bound for the density of dislocations at the shock front in these experiments, we estimate that the time-scale for propagating dislocations in Si is microseconds, whereas it is only tens of ps for Cu. The laser shock experiments are conducted with a ns time-scale, which means we expect to see a fully 3D relaxation in Cu, but not in Si. [12]

These results may also be consistent with the presence of a shock-induced phase transformation, or with a higher HEL for Si than previously reported. [22] There are several phase transitions that occur in Si in the pressure range from 11-20 GPa, [23, 24] and previous measurements of the wave breakout from shocked Si were consistent with the transition from diamond cubic structure to the β-tin structure at approximately 11 GPa. [22]

For the laser experiments, results from a pressure scaling experiment suggest that a phase transition occurs. For the lowest pressure case (9 GPa), the compression of the [004] planes was only a few percent, as illustrated by lineouts of the diffraction data shown in Fig. 9. At moderate pressure (11 GPa), multiple compressions were observed up to 6.4%. At higher pressures (>16 GPa), a single lattice compression of approximately 6.4% was observed. The fact that the compression remains at approximately 6.4% along the shock direction could correspond to the density at which a shock-induced phase transformation occurs, where the lattice spacing of the final state is not recorded, or the possibility that the HEL for Si is actually higher than previously reported.

A similar trend is observed with the VISAR wave profiles for Si. The free surface velocity is shown for 3 separate cases in Fig. 10. These represent shock drive pressures of 9, 16, and 22 GPa, as calculated using Lasnex based on the laser drive conditions. The peak particle velocity at initial breakout is expected to increase with pressure, however the initial breakout is unchanged at the higher pressure (22 GPa). The fact that the peak

free-surface velocity does not change with increasing pressure suggests that there is a transition from a single wave to a multiple wave structure, with a time-scale that is longer than a few ns. Based on the free surface velocity and breakout time of this first wave, we estimate the transition occurs at approximately 15 GPa, which is consistent with the Lasnex simulations for pressure, and much higher than the reported HEL of 9.2 GPa. [22]

In order to further study the response of the Si and other materials, a wide solid-angle collection detector was developed. This detector was developed to collect x-rays diffracted from multiple lattice planes. It consists of 3 separate static x-ray film holders that are held together to approximate a 90° segment of a sphere. The geometry of the full assembly is shown in Fig. 11. This detector was designed for experiments at the OMEGA, laser at the University of Rochester, and has also been used at the Janus laser at LLNL. We describe the details of how it is configured and fielded at OMEGA. The detector is positioned in the OMEGA target chamber by inserting it with a re-entrant manipulator, and held so that it surrounds target chamber center, subtending an angle of ≥90° in one direction and 180° in the other. The film is held at a distance of approximately 53 mm from target chamber center.

This instrument is used in combination with a target designed specifically for wide-angle diffraction. The target is illustrated in Fig. 12. It consists of a lead-doped plastic base plate that holds the single crystal sample, and a thin gold shield that holds a metal foil for the x-ray backlighter source. K-shell x-rays are created by 4-6 laser beams incident on the thin metal foil. A 200 μm diameter aperture in the backlighter shield defines the size of the source of x-rays.

The K-shell x-rays that diffract from the crystal are recorded on film. The direct line of sight to the film is blocked with a cylindrical shield placed above the 200 μm

aperture. This provides x-rays over a full π-solid angle that may be incident on the crystal and diffracted to the film.

Wide-angle measurements

This new detector has been fielded on a series of target experiments at OMEGA. A preliminary test was done with single crystal Cu. X-rays diffracted from approximately 12 different lattice planes of the static Cu sample were recorded on film simultaneously, as shown in Fig. 13. In this geometry, the crystal had a [001] orientation. It had an arbitrary orientation about the sample normal. A thin Cu foil was used for the x-ray source, providing x-rays with a wavelength of 1.49 Å. X-rays diffracted from the [002] planes have a Bragg angle of 24.36°, and from the [004] planes have a Bragg angle of 55.64°. Both of these are visible, along with x-rays diffracted from planes at an angle with respect to the crystal surface.

The different lines that are visible in this sample image are conic sections. Each results from a point source of x-rays diffracted from a single lattice plane and recorded on a flat piece of film. The geometry to illustrate this is shown in Fig. 14. In this illustration, x-rays diffracted from an arbitrary infinite lattice plane form the surface of a cone. The orientation of the lattice normal is the direction of the axis of the cone, and the Bragg angle for that lattice plane is 90 minus the half angle of the cone. The extent of the cone of x-rays diffracted from the crystal is determined by the angle that the crystal subtends to the x-ray source, and the appearance of the line on film is the intersection of this cone with the static film detector.

The process for identifying the lattice planes and extracting quantitative information on the shock response of the crystal is an iterative process that requires us to first identify the lattice planes, to transform the data to spherical coordinates, and then to fit the lattice planes for arbitrary diffraction signals.

The first step is to identify some of the lattice planes in the film data. This is done using an IDL code to calculate the expected signal from a given lattice plane. An x-ray source and lattice plane are input, and a diffraction pattern is calculated as an image that displays in spherical coordinates, theta and phi. An image that includes the diffraction signals from several different lattice planes may be calculated based on the selection rules for the particular crystal.

We show several calculated images in Fig. 15 for single crystal Cu. In this case, we show only the diffraction for the [002], [004], [±1,-1,3], [±113], and [±313] planes. Two cases are shown, for the rotation of the crystal oriented symmetrically with respect to the film, and for a slight offset rotation of 20°. By comparing the film images with the calculated diffraction patterns, a number of lattice planes are identified. These are then used to optimize the relative position of the target with respect to the film for the detailed lattice plane analysis.

In this case, the [002] and [004] planes are used. For an x-ray source with a wavelength of 1.49 Å, the Bragg angle for the [002] plane is 24.36°, and for the [004] plane is 55.64°. An IDL code is used to warp the film images to spherical coordinates based on geometrical inputs such as the position and angle of the crystal relative to the film. This transformation is optimized to match the Bragg angles for both the [002] and [004] planes. The optimum transformation is shown in Fig. 16 for the film images shown earlier in Fig. 13. Note that in spherical coordinates, the [002] and [004] planes are located at fixed values of theta.

The final step is to extract lattice information from other planes. This is done by identifying several points on each line, and fitting a conic section to those points. The parameters for this conic section then define the lattice plane. Specifically, the half-angle of the best-fit cone is 90-Bragg angle, and the axis of the cone is directed along the unit normal for the specific lattice plane (Fig. 14). Note that in this example of a static Cu crystal, the other planes should match the planes for single crystal Cu.

This new wide-angle film detector has been fielded on a series of target experiments at OMEGA. A series of experiments were done with shocked single crystal Si at the same conditions as for the VISAR wave profile measurements. The results obtained at 9 and 22 GPa are shown in Fig. 17. Here, we observe diffraction signals from both static and compressed lattice planes. In each case, the offset of each diffraction line is compared with calculations assuming only uniaxial compression. These images show the data on the left side, and simulations on the right.

At low pressure (9 GPa), diffraction from the all of the lattice planes shows a uniaxial compression of approximately 2% (Fig. 17a). And for the higher pressure case (Fig. 17b), all diffraction lines are consistent with a uniaxial compression of 6.4% along the shock direction [001]. This confirms that the lattice is responding elastically at a stress beyond the published HEL, and the time-scale for any transition at higher stress is longer than a few ns.

The single crystal Cu experiments have also been repeated with the wide-angle detector. In this case, 200 μm thick samples of Cu [001] were used. A total of 200 J of laser energy was incident on a 10 μm CH ablator on the front surface of the crystal in a 3.5 n pulse using a single beam with a 2.5 mm spot size. This generated a strong shock with a peak pressure of approximately 60 GPa that decayed as it propagated into the sample. Multiple beams from the OMEGA laser were used to create two separate x-ray pulses for the diffraction measurement. These were timed to probe the free surface of the crystal during the shock propagation (before breakout) to record the static diffraction pattern, and immediately before breakout when the bulk of the probe depth was compressed, as indicated in Fig. 18.

Many different lattice planes were recorded in these experiments using a Cu backlighter foil to generate x-rays at 1.49 Å. The images show x-rays diffracted from both the static and shocked lattice (Fig. 19). A calculation of the diffraction pattern from

the initial lattice is shown overlaid on the right. In this example, the diffraction pattern shows compression of several different lattice planes, but it is not spatially uniform. This may be due to structure in the shock front caused by non-uniformity of the laser focal spot on target and uncertainty in the shock breakout time.

Advanced concepts

The technique of probing many lattice planes simultaneously provides information on the configuration of the lattice during shock loading. In the experiments that we describe above, both the static and shocked lattice configurations were recorded. For these experiments, this was essential to account for variations in the position of the target sample from shot to shot. As a result, there is some ambiguity as to when each diffraction line was recorded on the film. This uncertainty may be reduced by using separate foils for the two backlighter pulses. By designing the target with two separate backlighter foils and apertures, images may be recorded at different times with different wavelength x-rays, as illustrated in Fig. 20. For example, Fe and Cu may be used to probe a sample of Cu [111]. In this case, the Bragg angle for the Fe x-rays is 62.8°, and for the Cu x-rays is 45.8°. The diffracted lines can be distinguished with differential filtering in the film assembly to allow detailed fitting of the static vs. compressed lattice.

The large-angle collection detector allows us to record x-rays diffracted from many different lattice planes. This may be used for poly-crystalline samples with large grains. Since the x-rays are incident at a wide range of angles on the crystal, this is not useful as a diagnostic of the detailed lattice structure for a poly-crystal material, but it does provide a diagnostic of the state of the material as evidenced by the existence of a lattice. This is demonstrated with images of poly-crystalline Be, shown in Fig. 21. A pattern of diffraction lines is evident, indicating that this material is solid during the experiment.

Molecular dynamics simulations

Diffraction from shocked single crystal copper shows that the crystal deforms in a manner apparently close to hydrostatic compression with a rapid (sub-nanosecond) compression of the lattice in directions both parallel and perpendicular to the shock front, consistent with the models of lattice deformation. Theoretical understanding of the response of crystals to shock compression has been significantly advanced by the advent of molecular dynamics (MD) calculations simulating the response of tens of millions of atoms for tens of picoseconds.

In this case, since the single crystal samples used in the laser experiments were very thin (as thin as 2-8 μm) compared to the transverse dimension (1 mm), this volumetric compression is a result of the local rearrangement of the lattice under compression due to the generation and propagation of dislocations. Given the time-scales of the experiment, we conclude that such rearrangement of the lattice can take place on sub-nanosecond time-scales which may be directly accessible to simulation by MD techniques.

Simulations were done with the code MDCASK [25], adapted to simulate shocks. An elongated box was equilibrated during several ps at 1.5 K, using periodic boundaries in only the x and y directions. In these non-equilibrium MD simulations, a step pulse shock wave was applied along the z direction as follows. An extra force was added to a few planes of atoms (typically 2-4 planes) on one side of the sample. The force was kept constant throughout the simulation, although a time dependent profile could be applied. Velocity profiles were analyzed at different times giving both the piston velocity, U_p, and the shock velocity, U_s. There was a transient stage, lasting around 1-2 ps, which was neglected in the shock velocity calculations. Shock profiles were sharp, allowing for

accurate determination of the shock speed. A plastic front was seen in the simulations only above a ``plastic threshold'' in the shock pressure of approximately 25-30 GPa.

Most non-equilibrium shock simulation studies to date have dealt with pair potentials, like Lennard Jones (LJ) [26-29], Morse, Buckingham, and others. Taylor and Dodson presented results on the Hugoniot of Cu for shocks along the <100> directions using an embedded-atom (EAM) potential, for U_p in the range 0-2.5 km/s and a target with 4 x 4 x 30 fcc unit cells [30]. Here we use a EAM parametrization by Mishin and coworkers [31]. Most simulations reported here were done for sample sizes of 50 x 50 x 200 fcc cells, i.e. 181 x 181 x 723 $Å^3$ and 2 x 10^6 atoms. Some results were obtained for smaller samples with 25 x 25 x 100 cells, and results for the elastic shock in these two sample sizes were indistinguishable for this potential.

This embedded atom potential model has been fitted to high pressure ab-initio simulations of the ``cold'' curve of Cu, i.e. the energy-volume relationship at 0 K, which is a useful feature for the shock simulations at high pressure. It has a stacking fault energy of 44.0 mJ/m^2 which compares well with experiments [31], and a cut-off radius that includes only 4 nearest neighbor shells. By using a non-zero stacking fault energy, there is a finite separation between the partial dislocations in the fcc crystal, namely around 2 nm for this EAM potential. In order for the lateral size of the target to accommodate this separation, at least 6 unit cells are required in the lateral direction for the potential used here.

When the piston is moved above a certain pressure, two shock fronts are produced. The first is the elastic front, which is also produced at lower pressures. The elastic front only compresses the lattice, creating few point defects due to large fluctuations near this front. The second shock front is the plastic front, which needs some threshold stress value to be initiated, as in the perfect LJ crystal [26].

Figure 22 shows a snapshot from the MD simulation of a 50 GPa shock, moving in the direction of the arrow, 7.8 ps after the shock started. Only a fraction of the sample is shown. The position of the elastic and plastic shock fronts are shown, with the plastic front about ten crystal planes behind the elastic front. The shock front is ``rough'' with a width of few atomic spacings, and supports large ``temperature'' and ``pressure'' gradients, making these thermodynamic variables difficult to define at small scales and indicating a non-equilibrium situation [32].

Figure 23 shows what happens when there is no plastic front produced. The elastic ``wave-train'' has been seen in LJ crystals simulations at 0 K [26]. The ``ringing'' of the velocity profile is produced by reverberations of adjacent planes. This effect is produced by the ABAB stacking of the 100 planes.

From the velocity profiles at different times one can calculate both U_p, and U_s. In this case the shock pressure is P_H=20 GPa, and U_s= 4.56 km/s; U_p= 0.44 km/s. Figure 24, on the other hand shows what happen for very strong shocks. The elastic front is almost 100% engulfed by the plastic front 3.2 ps after the shock was turned on. In this case the crystal behind the shock is molten, but the shock is propagating into a pristine crystal.

At pressures above elastic behavior shown in Fig. 23 and below the shock melting in Fig. 24, the plastic front nucleates dislocations as it travels through the pristine lattice. As a result, and due to the separation of partial dislocations by stacking faults (SF), a network of SF's is observed behind the shock front. Figure 25 shows this resulting defect structure, which is also seen in simulations using a short range LJ potential, where the SF energy is zero (the unstable SF energy is non-zero). The atoms associated with the SF's are highlighted using a potential energy filter. This is the same snapshot that is shown in Fig. 22, for a 50 GPa shock. The slip of the {111} planes can also be seen in Fig. 22 as a cross-hatch pattern behind the plastic front. The formation of

stacking faults has been identified as the main dislocation multiplication mechanism near the shock front by a recent model [9].

All the above results are for an initially perfect crystal, with no defects. However, even well annealed "single crystal" metals have a residual dislocation density. We are currently studying the influence of defects on the shock propagation and induced plasticity.

Simulated x-ray diffraction

X-ray diffraction post-processing is conceptually simple. The sample sizes used in the MD simulations are small enough that, even in the absence of dislocations, the diffraction is kinematic (ie. extinction can be ignored). Thus the intensity, I, of the diffracted radiation is given by

$$I = \left| \sum f_j \exp(i[r_j \cdot \Delta k]) \right|^2$$

where f_j is the atomic form factor of the j^{th} atom, r_j its position, and the Δk the difference between the wavevectors of the incident and scattered radiation. Absorption effects can be included by keeping track of the path length traversed by the x-rays scatter from a given atom, but current simulated sample sizes make this unnecessary.

It is of interest to compare the results of the diffraction experiments with the predictions of the MD calculations. A simple post-processor was written to produce diffraction patterns from the MD simulations for comparison with the experimental data. Initial results from this post-processor provide an indication of the future work required to make quantitative comparisons between MD simulations and experiments such as those described earlier.

Figure 26 shows the simulated diffraction signal from a sample of size 50 x 50 x 200 fcc unit cells. Intensity is plotted as a function of Δk, normalized to the length of the [001] reciprocal lattice vector. A snapshot was taken 7.81 ps after the start of the MD simulation, before the shock reached the rear surface. For clarity, the contribution to the diffraction signal from the unshocked region is not included. Diffraction peaks at Δk values corresponding to the allowed Miller indices are observed. Further, a noticeable shift in the lattice diffraction signal is observed, corresponding to the lattice compression along the shock propagation direction. In the second order, no observable shift can be seen in the diffraction from orthogonal planes, although some shift is evident in the fourth order. The observed angular shift of the second order peak suggests a compression of 16.5 ± 1.5 %, along [001] and of 0 ± 1.5% along [100] and [010]. The fourth order peak is more sensitive to compression in that Δk is proportional to the order of diffraction, however this signal also has more numerical noise. The shift of the fourth order peak suggests a compression of 13 ± 2%along [001] and 3.5 ± 2% along the orthogonal lattice directions.

Under the assumption of zero plastic dilatation the sum of the elastic strains in the three orthogonal directions should equal the volumetric compression. Thus, given the error bar associated with the shifts in the diffraction features, the observed elastic strains inferred from the diffraction pattern are consistent with the 18% compression deduced directly from the MD simulations. Note that although small shift in diffraction signals is seen corresponding to elastic strain orthogonal to the shock propagation direction, the dislocation density in the shocked region of the crystal is high, of the order of 10^{12} cm^{-2}.

Several forms of diffuse scattering may also occur, including non-specular diffraction due to the finite divergence of the diffracted radiation. In conventional dynamical diffraction theory for perfect crystals, non-divergent beams are assumed as

the rocking curve width is inversely proportional to the effective number of scatterers parallel to the reciprocal lattice vector of the diffracting planes. However, owing to the finite number of atoms in this simulation, the outgoing beam will diverge.

This is why the scattered intensity form the planes normal to the shock propagation direction differs from that in the orthogonal directions, These effects become less important as the scale of the simulations increases. More importantly, further reduction in the integrated intensity will occur due to the local rotations of the reciprocal lattice vectors which are associated with finite rotations of small regions of the lattice during the generation of dislocations. These factors will be taken into account in future simulations showing the effect of diffuse scattering and sample size on the error bars of elastic strains deducted form the diffraction pattern shifts.

A second source of diffuse scattering is due to thermal effects, such as the Debye-Waller effect. We do not expect this to be a large effect for the temperatures present here.

References

[1] P. England, and P. Molnar, Science **278**, 647 (1997).

[2] D. J. Steinberg and C. M. Lund, J. Appl. Phys. **65**, 1528 (1989).

[3] C. A. Hall, J. R. Asay, W. M. Trott, M. Knudson, K. J. Fleming, M. A. Bernard, B. F. Clark, .A. Hauer, G. Kyrala, Shock Compression of Condensed Matter – 1999, Edited by M. D. Furnish, L. C. Chhabildas, R. S. Hixson, (AIP New York, 2000) pp. 1171-4.

[4] D. H. Kalantar, B. A. Remington, J. D. Colvin, K. O. Mikaelian, S. V. Weber, L. G. Wiley, J. S. Wark, A. Loveridge, A. M. Allen, A. A. Hauer, M. A. Meyers, Phys. Plasmas **7**, 1999 (2000).

[5] D. J. Steinberg, S. G. Cochran, M. W. Guinan, J. Appl. Phys. **51**, 1498 (1980).

[6] L. C. Chhabildas, J. R. Asay, J. Appl. Phys. **50**, 2749 (1979).

[7] Q. Johnson, A. Mitchell, and L. Evans, Nature (London) 231, 310 (1971); Q. Johnson, A. Mitchell, and L. Evans, Appl. Phys. Lett. 21, 29 (1972).

[8] J. S. Wark, R. R. Whitlock, A. A. Hauer, J. E. Swain, and P. J. Solone, Phys Rev B 40, 5705 (1989).

[9] E. Zaretsky, J. Appl. Phys. **78**, 1 (1995);

[10] P. A. Rigg and Y. M. Gupta, Appl. Phys. Lett. **73**, 1655 (1998).

[11] D. H. Kalantar, E. A. Chandler, J. D. Colvin, R. Lee, B. A. Remington, S. V. Weber, L. G. Wiley, A. Hauer, J. S. Wark, A. Loveridge, B. H. Failor, M. A. Meyers, G. Ravichandran, Rev. Sci. Instrum. **70**, 629 (1999).

[12] A. Loveridge-Smith, A. Allen, J. Belak, T. Boehly, A. Hauer, B. Holian, D. Kalantar, G. Kyrala, R. W. Lee, P. Lomdahl, M. A. Meyers, D. Paisley, S. Pollaine, B. Remington, D. C. Swift, S. Weber, J. S. Wark, Phys. Rev. Letters **86**, 2349 (2001).

[13] M. A. Meyers, F. Gregori, B. K. Kad, M. S. Schneider, D. H. Kalantar, B. A. Remington, J. S. Wark, T. Boehly, G. Ravichandran, Shock Compression of Condensed Matter – 2001, Edited by M. D. Furnish, N. N. Thadhani, and Y. Horie, (AIP New York, 2002) pp. 619-622;.

[14] Marc A. Meyers, F. Gregori, B. K. Kad, M. S. Schneider, D. H. Kalantar, B. A. Remington, G. Ravichandran, and T. Boehly, "*Laser-Induced Shock Compression of Monocrystalline Copper: Characterization and Analysis*", Acta Materialia **51**, 1211 (2003).

[15] M. S. Schneider, B. K. Kad, F. Gregori, D. Kalantar, B. A. Remington, M. A. Meyers, "*Laser-induced shock compression of copper: orientation and pressure decay effects*", to appear in Metallurgical and Materials Transactions.

[16] L. E. Murr in Shock Waves and High-Strain-Rate Phenomena in Metals, M. A. Meyers, and L. E. Murr, Eds., Plenum, New York, NY, 1981, pp. 607-673.

[17] O. Jahari and G. Thomas, Acta Metal. **12**, 1153 (1964).

[18] Gray III, G.T., in *Shock-Wave and High-Strain-Rate Phenomena in Materials*, eds. M.A. Meyers, L.E.Murr, and K.P. Staudhammer, M. Dekker, NY, 1992, p. 899.

[19] D. M. Gold, P. M. Celliers, G. W. Collins, L. B. DaSilva, R. C. Cauble, D. H. Kalantar, S. V. Weber, B. A. Remington, Shock Compression of Condensed Matter – 1999, Edited by M. D. Furnish, L. C. Chhabildas, R. S. Hixson, (AIP New York, 2000) pp. 1007-10.

[20] D. H. Kalantar, A. M. Allen, F. Gregori, B. Kad, M. Kumar, K. T. Lorenz, A. Loveridge, M. A. Meyers, S. Pollaine, B. A. Remington, J. S. Wark, Shock Compression of Condensed Matter – 2001, Edited by M. D. Furnish, N. N. Thadhani, and Y. Horie, (AIP New York, 2002) pp. 615-618.

[21] D. Hull and D. J. Bacon, Introduction to Dislocations (Butterworth-Heinemann, Oxford, 1984), p. 59.

[22] W. H. Gust and E. B. Royce, J. Appl. Phys. **42**, 1897 (1972).

[23] H. Olijnyk, S. K. Sikka, W. B. Holzapfel, *Physics Letters* **103A**, 137 (1984).

[24] J. Crain, G. J. Ackland, J. R. Maclean, R. O. Piltz, P. D. Hatton, G. S. Pawley, *Phys. Rev. B* **50**, 13043 (1994).

[25] T. Diaz de la Rubia and M. W. Guinan, Mat. Res. Forum **174**, 151 (1990).

[26] B.L. Holian and P.S. Lomdahl, Science **80**, 2085 (1998).

[27] V. V. Zhakhovskii, S. V. Zybin, K. Nishihara, and S. I. Anismov, Phys. Rev. Lett. **83**, 1175 (1999).

[28] T. C. Germann, B. L. Holian, P. S. Lomdahl, and R. Ravelo, Phys. Rev. Lett. **84**, 5351 (2000).

[29] J.-B. Maillet, M. Mareschal, L. Soulard, R. Ravelo, P. S. Lomdahl, T. C. Germann, and B. L. Holian, Phys. Rev. E **63**, 016121 (2001).

[30] P. A. Taylor and B. W. Dodson, Phys. Rev. Dodson, Phys. Rev. B **42**, 1200 (1990).

[31] Y. Mishin, M. J. Mehl, D. A. Papaconstantopoulos, A. F. Voter, and J. D. Kress, Phys. Rev. B **63**, 224106 (2001).

[32] F. J. Urebe, R. M. Velasco, and L. S. Garcia-Coli, Phys. Rev. B **58**, 3209 (1998).

Figures:

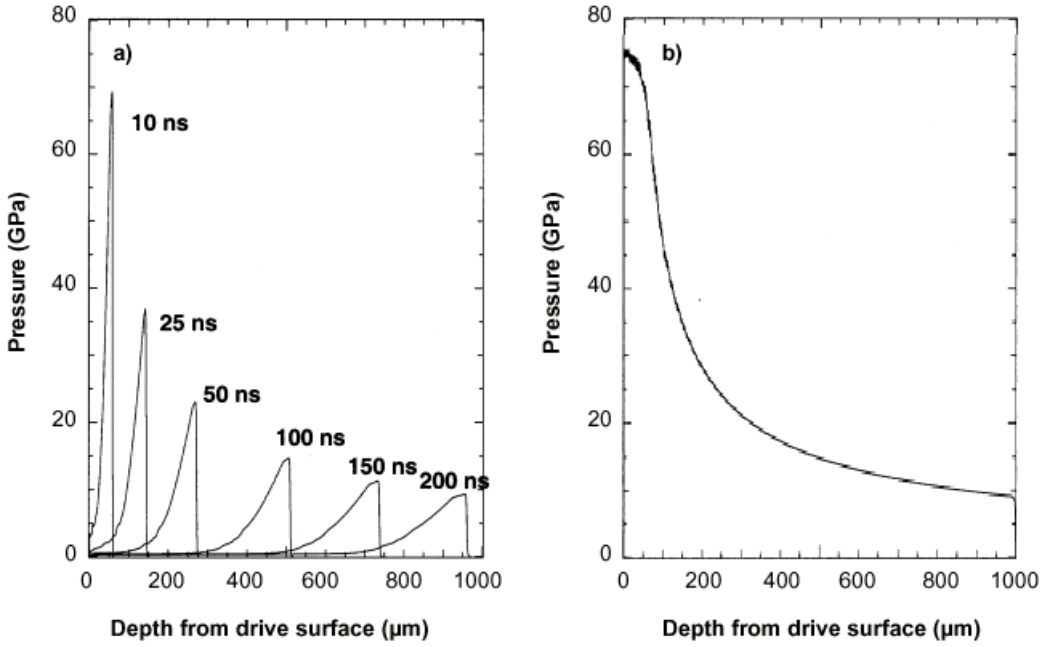

Figure 1: a) Pressure profile in 1 mm thick Cu plotted at various times. b) Peak stress as a function of depth in a 1 mm thick Cu sample. The pressure decays due to the release from the drive side as the laser turns off.

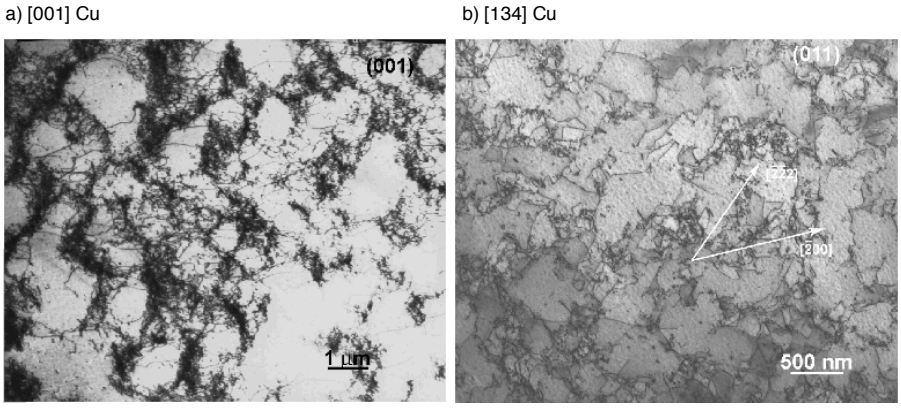

Figure 2: Defect substructures of monocrystalline copper shocked a) along the [001] direction, and b) along the [134] direction with approx. 70 J of laser energy showing a cellular structure of dislocations.

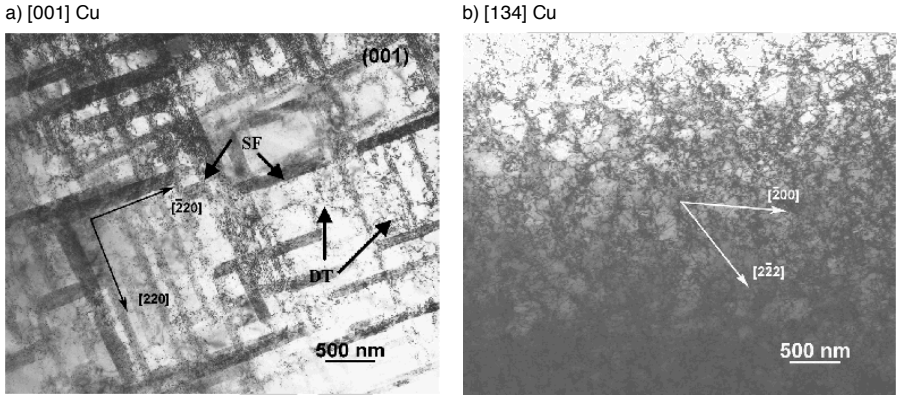

Figure 3: Defect substructures of monocrystalline copper shocked a) along the [001] direction, and b) along the [134] direction with approx. 200 J of laser energy. The structure in the [001] Cu is dominated by stacking faults, while the [134] Cu shows a dense network of dislocation cells approx. 150 nm in size.

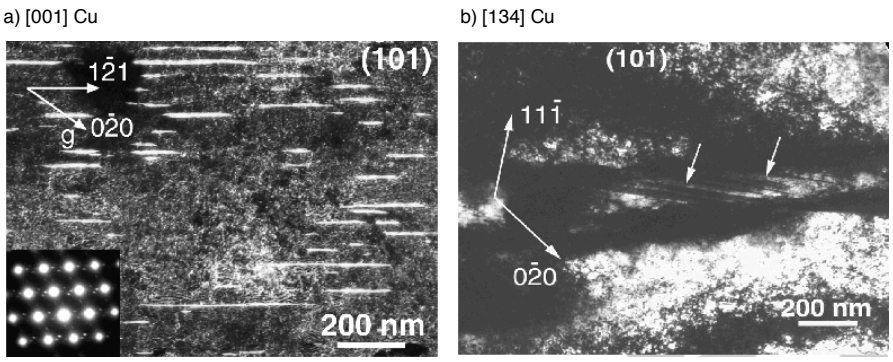

Figure 4: Defect substructures of monocrystalline copper shocked along the [001] direction with approx. 300 J of laser energy. These images show a) a large density of micro-twins, and b) micro-twins contained within wavy grain lath features.

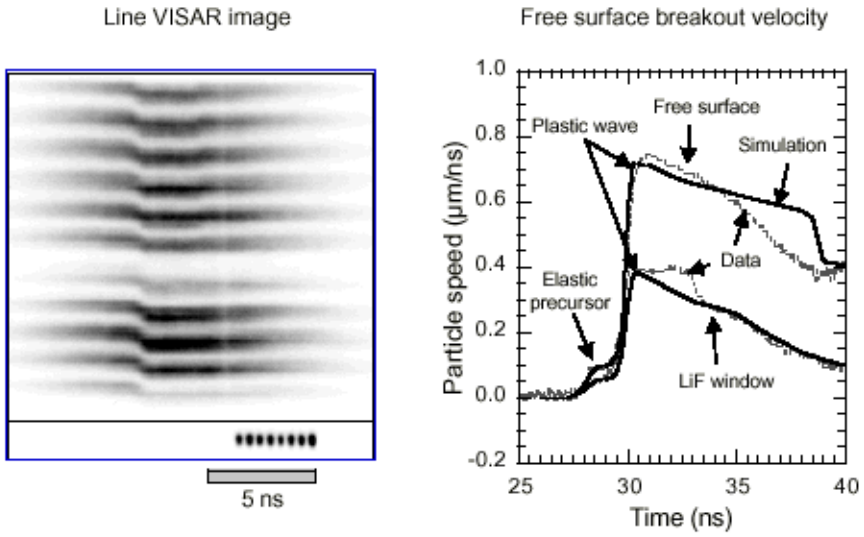

Figure 5: VISAR wave profile data from Al-6061 shocked at a peak pressure of approximately 2.7 GPa. This is spatially resolved over a 0.5 mm region on the target. Best-fit simulations are shown.

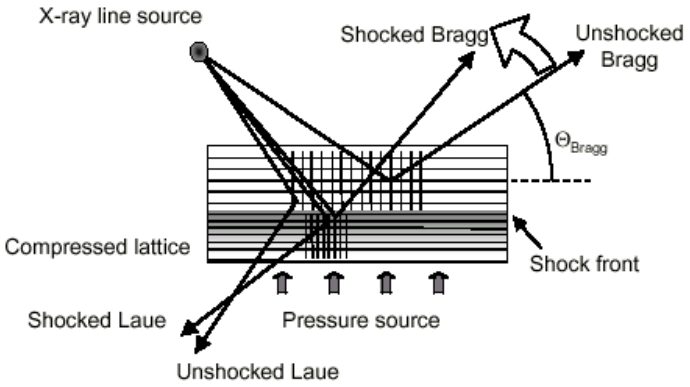

Figure 6: Geometry for in-situ x-ray diffraction. The diffraction x-ray source is located close to the sample so that the monochromatic x-rays are incident at a wide range of angles.

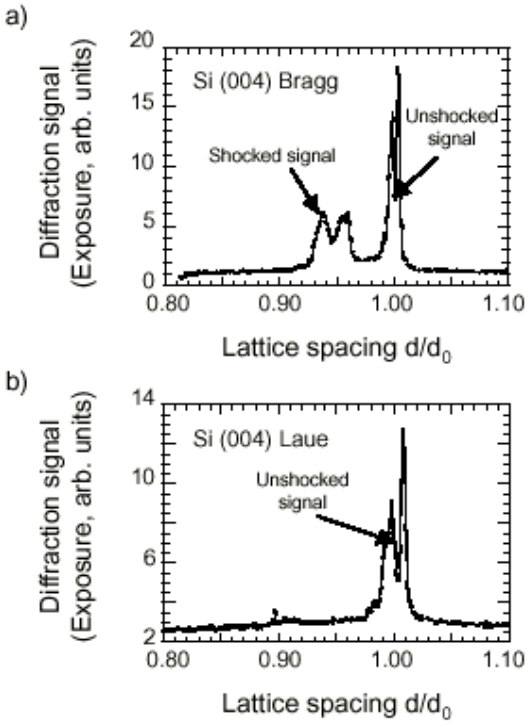

Figure 7: Diffraction measurements from single crystal Si shock compressed using a laser driver. The Bragg signal (a) shows compression of the lattice by approximately 6% along the shock direction. The Laue signal (b) shows no reduction of the lattice spacing in the direction orthogonal to the shock propagation.

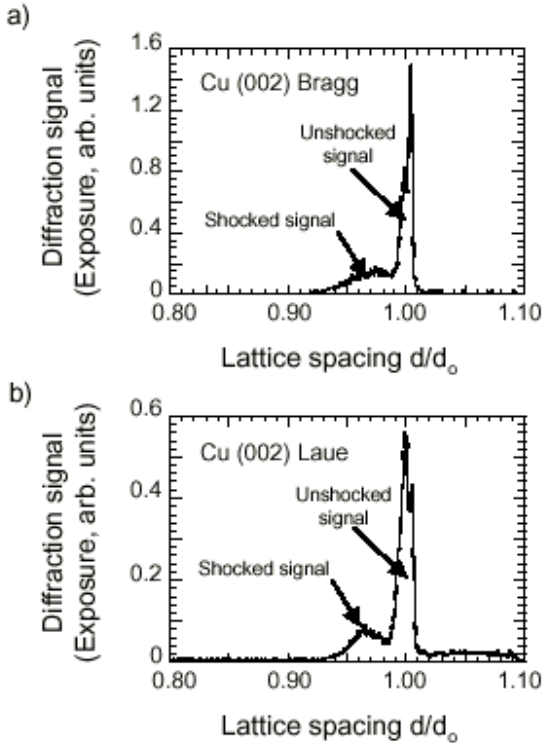

Figure 8: Diffraction measurements from single crystal Cu shock compressed using a laser driver. The Bragg signal (a) shows compression of the lattice of approximately 3% along the shock direction. The Laue signal (b) also shows compression of the lattice of approximately 3%.

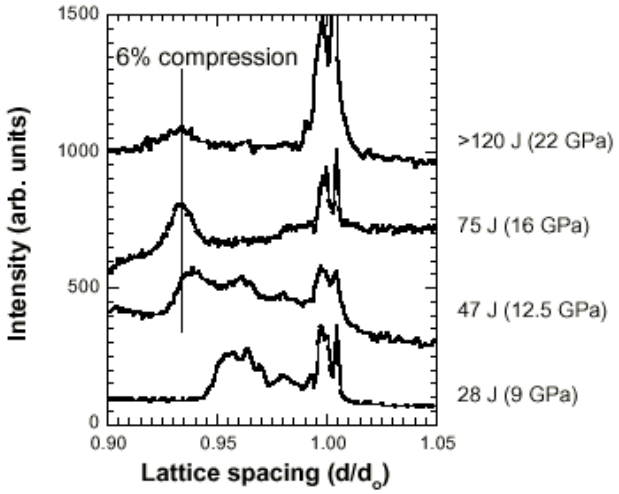

Figure 9: Lineouts of the compression measured in Si shock experiments at a range of pressures from 9-22 GPa. The peak compression of the (004) lattice planes appears to be limited to 6.4% at a range of pressures.

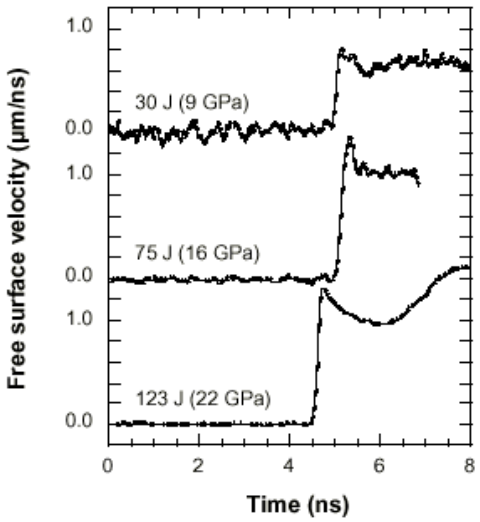

Figure 10: VISAR wave profile measurements from 40 μm thick single crystal Si shocked at pressures of 9-22 GPa using a 3.5 ns laser pulse. The particle velocity on release appears to be limited at 1.2 μm/ns over a range of pressures.

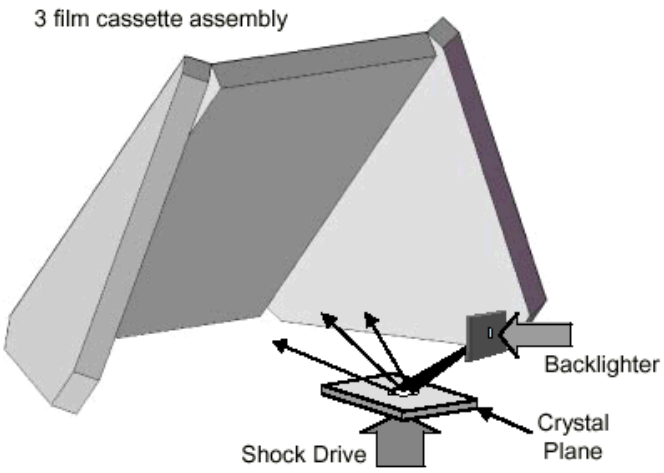

Figure 11: Geometry of the wide-angle film detector. This consists of 3 separate film holders that subtend a full π-steradian solid angle about the diffraction target.

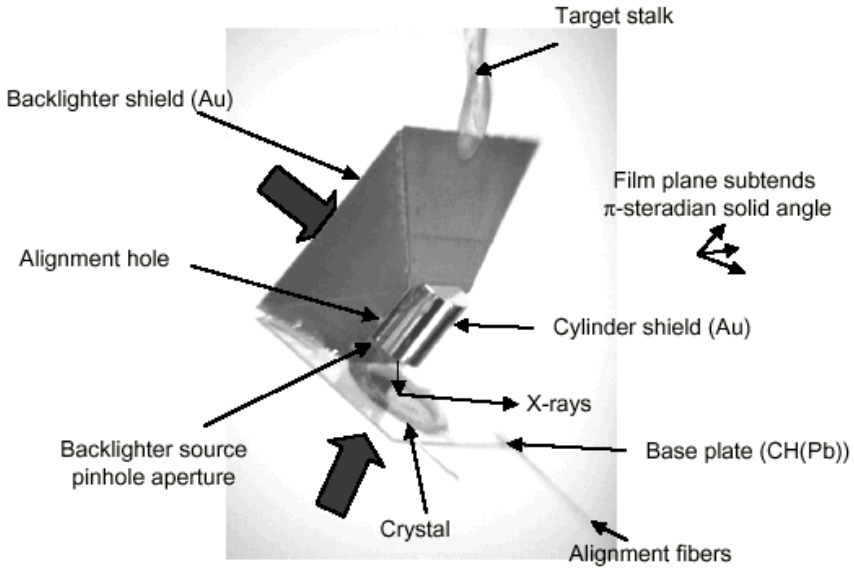

Figure 12: Photograph of a diffraction target used at OMEGA. The 3 mm diameter crystal is held behind the plastic base plate. The gold shields block the direct line of sight to the detector. X-rays that diffract from the crystal are recorded on the film.

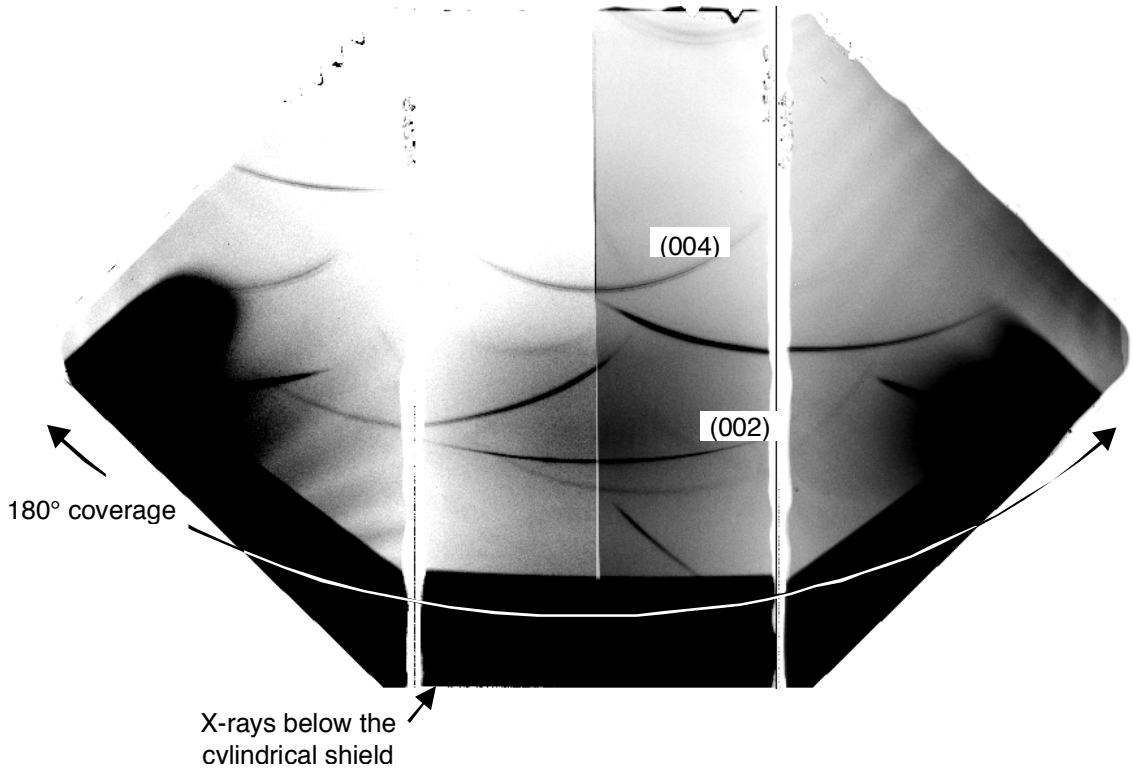

Figure 13: Example of the film data showing x-rays diffracted from multiple lattice planes of single crystal Cu. The (002) and (004) planes parallel to the surface are indicated.

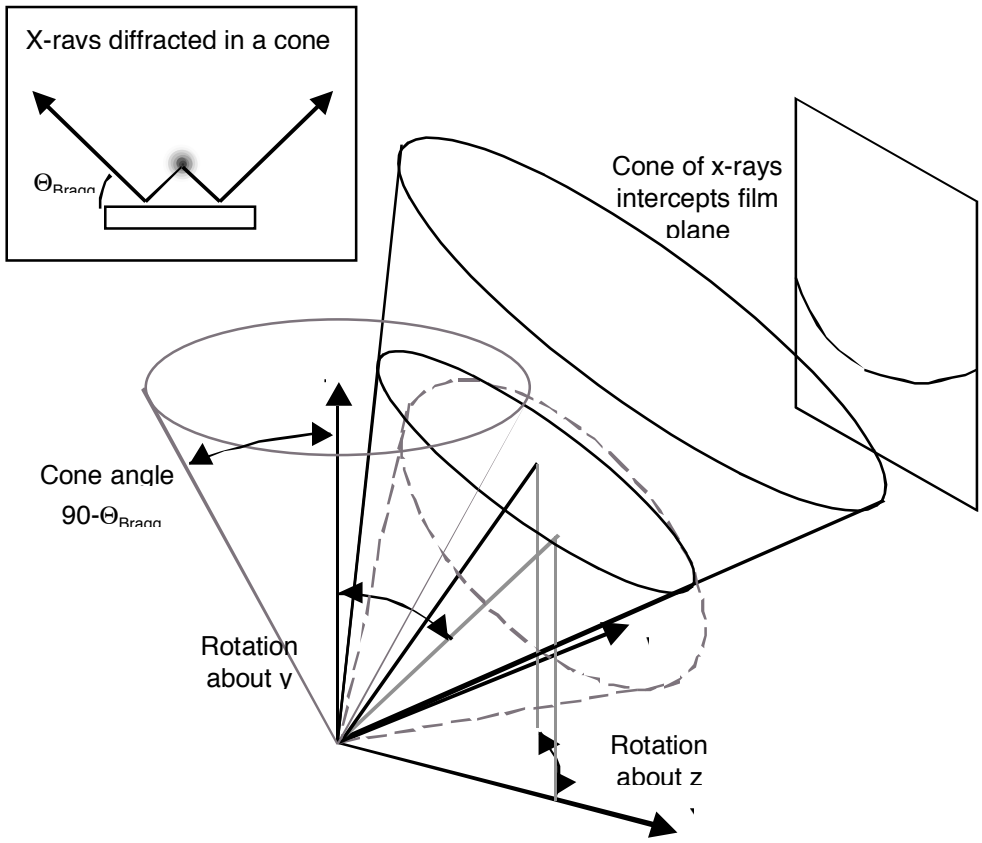

Figure 14: Geometry that is used in the fit routines for the diffraction signals. Each arc on film is due to a cone of x-rays diffracted from a specific lattice plane in the crystal. The best fit cone for each line is given by 3 angle parameters that represent the Bragg angle and lattice normal vector.

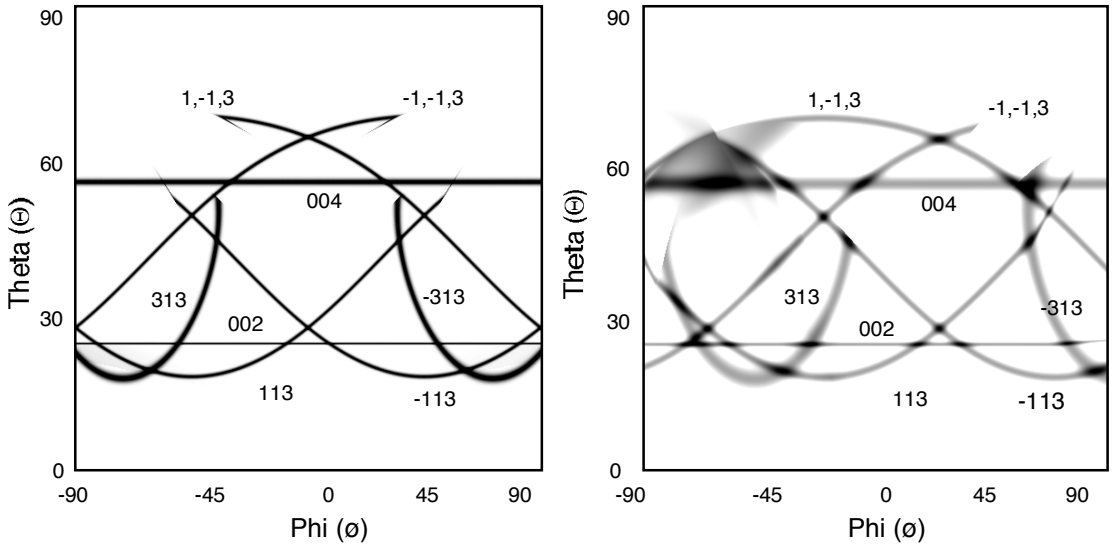

Figure 15: Calculated diffraction signals for specific lattice planes of single crystal Cu using a Cu x-ray source at 1.49Å. The relative orientation of the lattice is rotated by 20° for the image on the right.

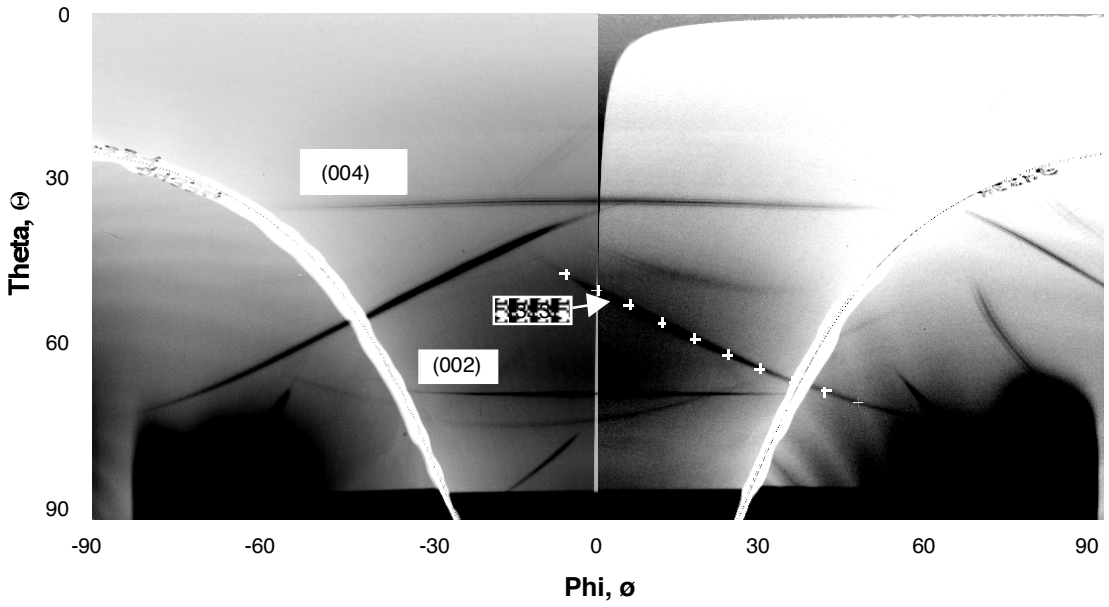

Figure 16: Warped image of the x-rays diffracted from single crystal Cu displayed in angle space. The data covers an angular range of 90° in the vertical direction and 180° in the horizontal direction.

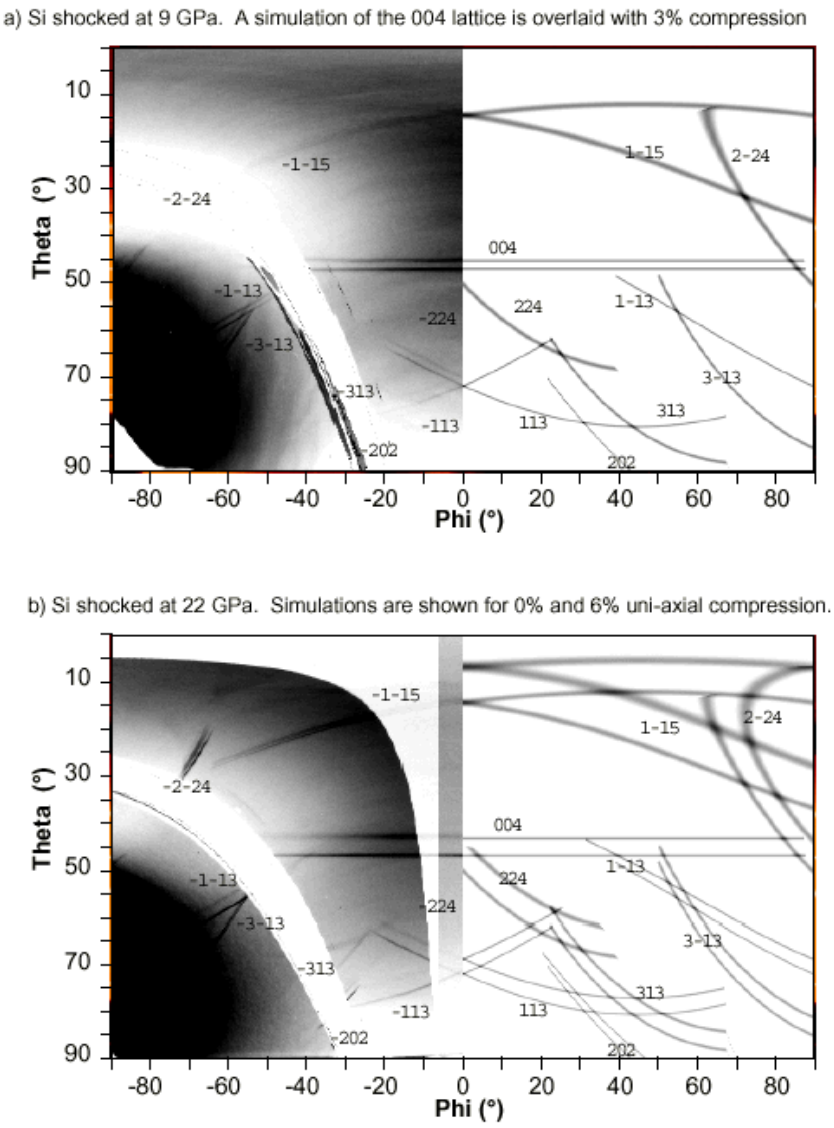

Figure 17: In-situ x-ray diffraction data from shocked single crystal Si (001). The data is displayed in spherical coordinates in the left half of the images, with simulations for the static, 3% and 6% uniaxial compressed lattice shown in the right half of the images. Data for shock pressures of a) 9 GPa and b) 22 GPa are shown.

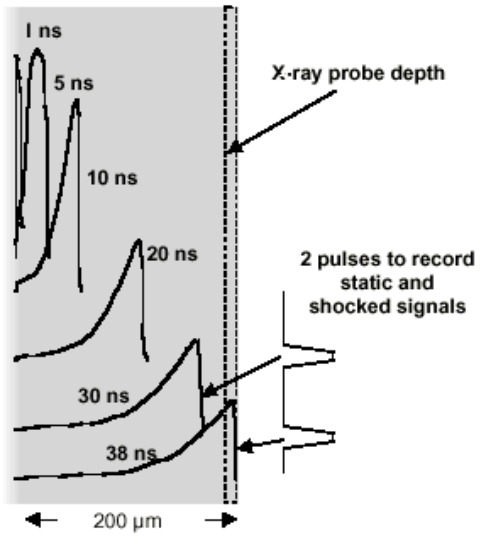

Figure 18: Pressure profile in a 200 μm thick single crystal Cu (001) sample at various times. Two separate backlighter pulses were timed with respect to shock breakout to record x-rays diffracted from both the static and compressed lattice.

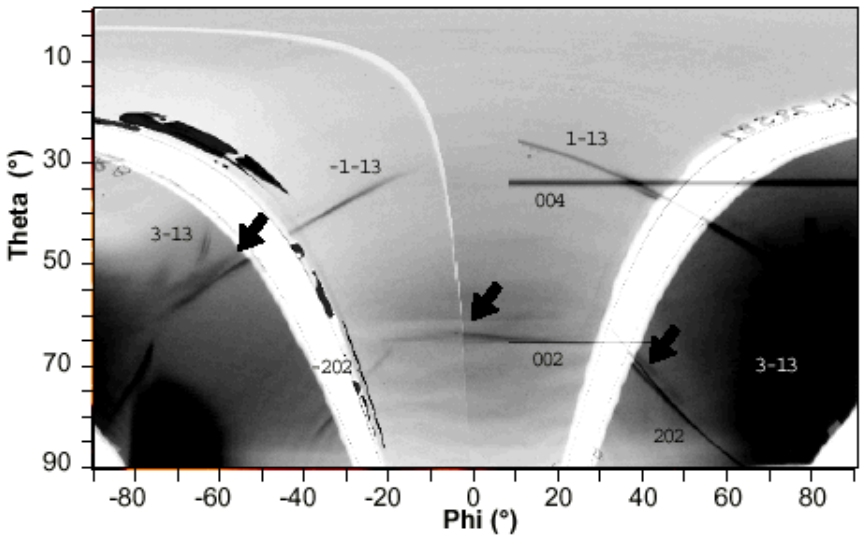

Figure 19: In-situ x-ray diffraction data from shocked 200 μm thick single crystal Cu (001). The backlighter was timed at 35 and 37 ns after the start of the laser pulse to capture full compression before shock breakout.

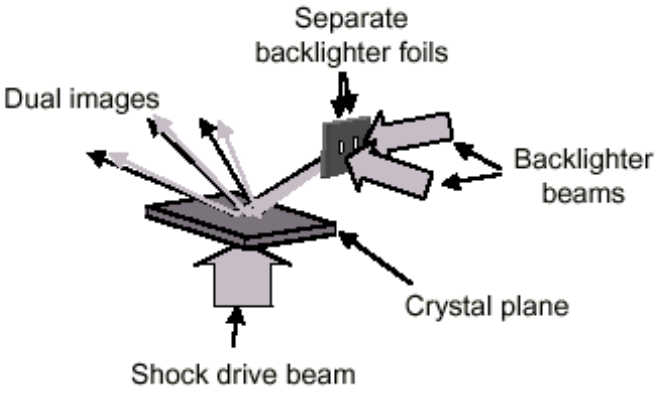

Figure 20: Schematic for in-situ diffraction using a dual backlighter to remove timing uncertainty from the data.

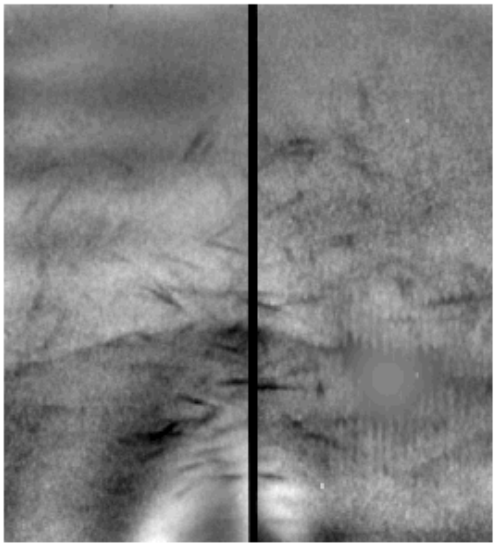

Figure 21: Example of in-situ diffraction data from a sample of poly-crystalline Be. The presence of diffraction lines from the multiple crystals demonstrates the phase of the sample.

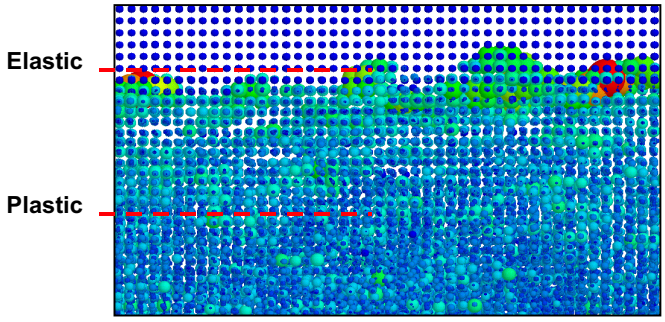

Figure 22: Snapshot of a subset of a MD simulation where a 50 GPa shock was launched in single crystal Cu. The image is shown 7.8 ps after the shock is launched.

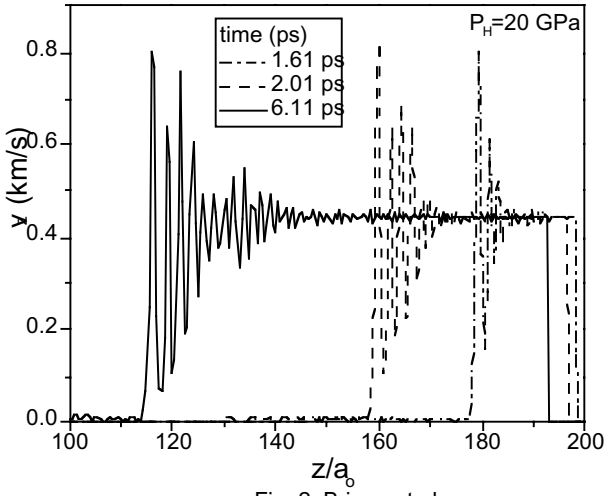

Figure 23: Velocity vs. depth at four different times for a 20 GPa shock. There is a train of elastic waves with no evidence of a plastic shock.

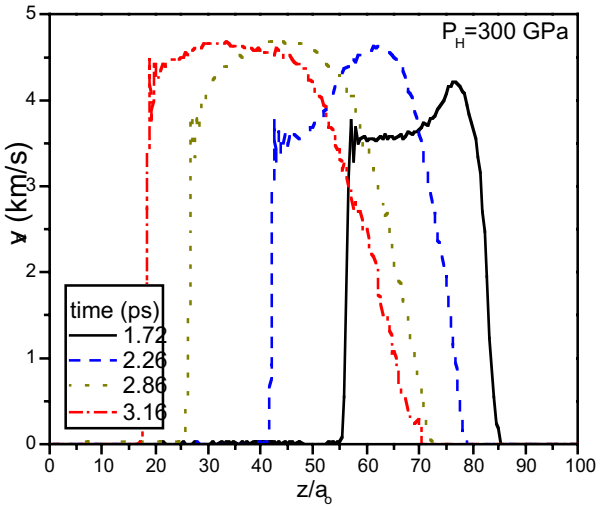

Figure 24: Velocity vs. depth at four different times for a 300 GPa shock. These profiles show the elastic shock front being overtaken by a plastic front.

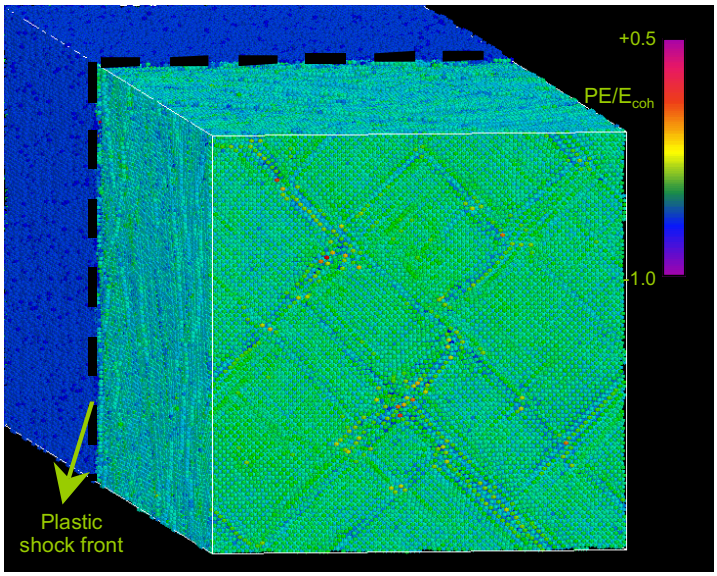

Figure 25: Potential energy snapshot of an MD simulation for a 50 GPa shock. The color scale is proportional to potential energy. Plastic deformation occurs in this simulation by formation of stacking faults that appear as a cross-hatch pattern in the image.

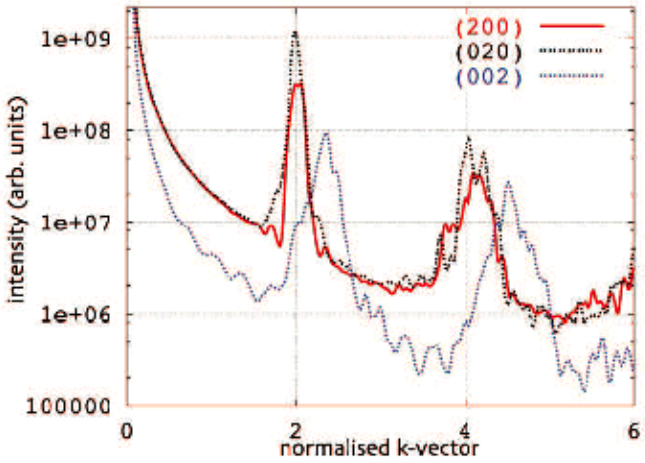

Figure 26: Diffraction intensity as a function of Δk normalized to the length of the [001] reciprocal lattice vector. The signature of compression along the shock propagation direction is evident, with less compression in the two orthogonal directions.

Acknowledgements

This work was performed under the auspices of the United States Department of Energy by the University of California Lawrence Livermore National Laboratory under Contract No. W-7405-Eng-48. The x-ray diffraction experiments were performed on Nova through the Science Use of Nova Program and on OMEGA through the National Laser User Facility Program.

Collaborators on this project included participants from both inside the laboratory and outside. The list includes the following:

D. H. Kalantar	National Ignition Facility Programs, LLNL
J. Belak	Physics and Advanced Technologies, LLNL
E. Bringa	Chemistry and Materials Science, LLNL
K. Budil	Chemistry and Materials Science, LLNL
J. Colvin	Chemistry and Materials Science, LLNL
M. Kumar	Chemistry and Materials Science, LLNL
R. Rudd	Physics and Advanced Technologies, LLNL
J. Stolken	Engineering, LLNL
K. Rosolankova	Clarendon Laboratory, University of Oxford
J. S. Wark	Clarendon Laboratory, University of Oxford
M. A. Meyers	Department of Mechanical and Aerospace Engineering, UCSD
M. Schneider	Department of Mechanical and Aerospace Engineering, UCSD

Publications

E. M. Bringa, M. Duchaineau, K. Rosolankova, R.E. Rudd, D.H. Kalantar, B.A. Remington, J.S. Wark, and J. Belak, "*Shock deformation of fcc metals on sub-nanosecond time scales*", in preparation.

M. S. Schneider, B. K. Kad, F. Gregori, D. H. Kalantar, B. A. Remington, M. A. Meyers, "*Laser-induced shock defects in copper aluminum alloys: stacking fault energy effects on the slip-twinning transition*", in preparation.

M. S. Schneider, B. K. Kad, F. Gregori, D. Kalantar, B. A. Remington, M. A. Meyers, "*Laser-induced shock compression of copper: orientation and pressure decay effects*", to appear in Metallurgical and Materials Transactions.

V. Lubarda, Ms. S. Schneider, D. H. Kalantar, B. A. Remington, M. A. Meyers, *"Void growth by dislocation emission"*, to appear in Acta Materialia.

J. Hawreliak, K. Rosolankova, B. Lings, F. Kerr, J. S. Wark, D. Kalantar, D. M. Chambers, A. D. Nask, N. C. Woolsey, "*Measurement of multiple plane diffraction from shock compressed crystals*", Central Laser Facility Annual Report 2002-3003, RAL-TR-2003-018, 54 (2003).

K. Rosolankova, D. H. Kalantar, J. F. Belak, E. M. Bringa, M. J. Caturla, J. Hawreliak, B. L. Holian, K. Kadau, P. S. Lomdahl, T. C. Germann, R. Ravelo, J. Sheppard, J. S. Wark, *"X-ray diffraction from shocked crystals: Experiments and predications of molecular dynamics simulations"*, submitted for the proceedings of the APS SCCM Meeting (July 2003).

B. A. Remington, G. Bazan, J. Belak, E. Bringa, M. Caturla, J. D. Colvin, M. J. Edwards, S. G. Glendinning, D. Ivanov, B. Kad, D. H. Kalantar, M. Kumar, B. F. Lasinski, K. T. Lorenz, J. M. McNaney, D. D. Meyerhofer, M. A. Meyers, S. M. Pollaine, D. Rowley, M. Schneider, J. S. Stolken, J. S. Wark, S. V. Weber, W. G. Wolfer, B. Yaakobi, *"Material Science at the extremes of pressure and strain rate"*, submitted for the proceedings of the TMS meeting (March, 2003).

M. A. Meyers, M. S. Schneider, B. K. Kad, V. A. Lubarde, F. Gregori, D. H. Kalantar, B. A. Remington, *"Laser shock compression of copper monocrystal: Mechanisms for dislocation and void generation"*, J. Phys. IV France **110**, 851 (2003).

D. H. Kalantar, J. Belak, E. Bringa, K. Budil, M. Caturla, J. Colvin, M. Kumar, K. T. Lorenz, A. M. Allen, K. Rosolankova, J. S. Wark, M. A. Meyers, M. Schneider, "*High pressure, high strain rate lattice response of materials*", Physics of Plasmas **10**, 1569 (2003).

Daniel H. Kalantar, E. Bringa, M. Caturla, J. Colvin, K. T. Lorenz, M. Kumar, J. Stolken, A. M. Allen, K. Rosolankova, J. S. Wark, M. A. Meyers, M. Schneider, T. R. Boehley, "*Multiple Film Plane Diagnostic for Shocked Lattice Measurement*", Rev. Sci. Instrum **74**, 1929 (2003).

E. M. Bringa, B.D. Wirth, M.J. Caturla, J. Stolken, and D. Kalantar, "*Metals far from equilibrium: from shocks to radiation damage*", Nuclear Instruments and Methods in Physics Research B **202**, 56 (2003).

Marc A. Meyers, F. Gregori, B. K. Kad, M. S. Schneider, D. H. Kalantar, B. A. Remington, G. Ravichandran, and T. Boehly, "*Laser-Induced Shock Compression of Monocrystalline Copper: Characterization and Analysis*", Acta Materialia **51**, 1211 (2003).

M. A. Meyers, F. Gregori, B. K. Kad, M. S. Schneider, D. H. Kalantar, B. A. Remington, J. S. Wark, and T. Boehly, G. Ravichandran, *"Plastic deformation in laser-induced shock compression of monocrystalline copper"*, Proceedings of the APS Topical Conference on Shock Compressed Condensed Matter, Atlanta, GA, 2001, AIP Conference Proceedings **620**, M. D. Furnish, N. N. Thadani, Y. Horie, Eds. (AIP, Mellville, NY, 2002) pp. 619-622.

D. H. Kalantar, A. M. Allen, F. Gregori, B. Kad, M. Kumar, K. T. Lorenz, A. Loveridge, M. A. Meyers, S. Pollaine, B. A. Remington, J. S. Wark, *"Laser driven high pressure, high strain rate materials experiments"*, Proceedings of the APS Topical Conference on Shock Compressed Condensed Matter, Atlanta, GA, 2001, AIP Conference Proceedings **620**, M. D. Furnish, N. N. Thadani, Y. Horie, Eds. (AIP, Mellville, NY, 2002) pp. 615-618.